Wear 560–561 (2025) 205622

Contents lists available at ScienceDirect

Wear

journal homepage: www.elsevier.com/locate/wear

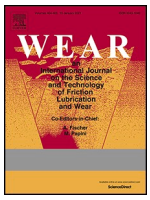

# Wear and damage behaviors of wheel-rail with different material matchings under various sand deposition densities of rail top in desert environments

K. Shu [a], N. Zani [b], L. Ghidini [b], C. Petrogalli [b], L.L. Yu [a], A. Mazzù [b,*], H.H. Ding [c], W.J. Wang [c]

[a] College of Mechanical Engineering, Hunan Institute of Science and Technology, Yueyang 414006, China
[b] Department of Mechanical and Industrial Engineering, University of Brescia, Brescia 25123, Italy
[c] Tribology Research Institute, State Key Laboratory of Rail Transit Vehicle System, Southwest Jiaotong University, Chengdu 610031, China

ARTICLE INFO

*Keywords:*
Desert environment
Sand deposition density
Wear
Damage
Wheel-rail

ABSTRACT

In desert environments, the phenomenon of sand particles depositing on the rail top and contaminating the wheel-rail interface is common because the railway is an open system. This work aimed to investigate the wear and damage behaviors of wheel-rail with different material matchings under various sand deposition densities of rail top in desert environments. The results showed that as sand deposition density increased, adhesion coefficient first decreased sharply and then increased slowly, and finally decreased slowly. It was caused by the combined effect of sand solid lubrication, oxide solid lubrication, and surface roughness of wheel and rail. The oxidative wear increased first, peaking at about 0.2 g/m$^2$, and then decreased, whereas the fatigue wear decreased consistently. For wheel and rail materials with similar hardness, the wheel-rail material matching with high carbon content exhibited excellent anti-wear and anti-fatigue performances. The wear and damage of wheel and rail were relatively mild when the sand deposition density was lower than 0.4 g/m$^2$.

## 1. Introduction

With the rapid development of railways in the world, the mileage of railway lines crossing the desert areas has been increasing gradually [1–3]. Simultaneously, the influence of sand hazards on railway transportation is also being reported more frequently, especially during the season of frequent dust storms. As shown in Fig. 1a, the phenomenon of track buried by desert sand is common in severe sand hazard regions because the railway is an open system. It is inevitable that some sand particles deposit on the rail top in desert railways. Subsequently, these sand particles will be rolled by the wheels of running trains. After the long-term service under the sand hazard regions, the rail surface becomes rough and the rail base rust, as shown in Fig. 1b. The wheel tread becomes rough and forms the hollow wear, as shown in Fig. 1c. The excessive wear and damage phenomena of wheel and rail in desert environments has been reported widely [3–7].

At present, the influence of sand particles in desert environments on the adhesion, wear and damage behaviors of wheel and rail in dry conditions have been studied by a few researchers using a twin-disc test machine. In general, the adhesion coefficient declined significantly when sand particles entered the wheel-rail surface, which was mainly attributed to the solid lubrication effect of sand particles and their fragments [10,11]. Furthermore, the presence of sand also markedly aggravated the wear and damage of wheel/rail materials. The wear mechanisms mainly included abrasive wear and ratcheting wear or fatigue wear. Grieve et al. [11] suggested that the excessive wear of the harder material was mainly caused by the scratching effect of the particles embedded in the surface of the softer material, whereas Faccoli et al. [10] found that in addition to abrasive wear, the surface crack was filled by sand fragments and formed the crack network speedily, and eventually resulted in the material detachment easily, which was another crucial reason for the excessive wear phenomenon. Subsequently, Mazzù et al. [12–14] used the numerical simulation method to further clarify the mechanical behaviors between sand fragments and wheel-rail interface. It was found that the presence of the sand fragments significantly increased the stress and strain peaks of the wheel-rail contact, which accelerated the wear and damage of the wheel-rail material under the ratcheting effect. In addition, Shu et al. [15] studied the effect of dynamic windblown sand environment on the wear and damage of wheel and rail using experimental method. The results indicated that although the adhesion coefficient could not be affected significantly, the combined effect of wind and desert sand could cause the obvious oxidative wear in addition to abrasive wear and fatigue wear. However, the above studies were conducted at a fixed sand feed rate or

* Corresponding author.
*E-mail address:* angelo.mazzu@unibs.it (A. Mazzù).

https://doi.org/10.1016/j.wear.2024.205622
Received 24 July 2024; Received in revised form 22 October 2024; Accepted 1 November 2024
Available online 4 November 2024

sand contamination level, and did not take into account the different degrees of sand contamination on rail top in desert environments. Therefore, the effect of sand contamination on rail top with different degrees on wear and damage of wheel and rail is still unclear and needs to be further investigated.

On the other hand, the service performances of different wheel and rail materials in desert environments have also been investigated seldomly using the twin-disc machine. Faccoli et al. [10,16] reported that the wheel material with higher cyclic yield stress and ductility exhibited better anti-wear and anti-fatigue performances in the presence of desert sand. Shu et al. [17] found that although the anti-wear performance could not be influenced noticeably by rail hardness in the dynamic windblown sand environment, the rail material with higher hardness presented better anti-fatigue performance. These findings indicated that the relationship between anti-wear and anti-fatigue performances and the mechanical properties of wheel/rail materials could be changed by the invasive sand particles in the desert environment. However, it is also unclear whether the anti-wear and anti-fatigue performances of different wheel-rail materials or matchings could be affected by varying degrees of sand contamination on rail top.

Therefore, the purpose of this work is to explore the wear and damage behaviors of wheel-rail with different material matchings under the sand contamination on rail top with various degrees in desert environments. Since there is currently no terminology to express the contamination degree of sand contamination on rail top in desert environments. Therefore, the term “sand deposition density”, defined as the mass of sand deposited per unit area ($\rho_D$, g/m$^2$), is used here to describe the contamination degree of rail top by sand deposition based on the similar definition in other references [18,19]. Wear and rolling contact fatigue tests of different wheel-rail material matchings under various sand deposition densities were conducted using a twin-disc machine. The adhesion, wear and damage behaviors of wheel and rail steels were analyzed by various characterization methods. The adhesion transition mechanisms under different sand deposition densities were proposed based on the analysis of results. The anti-wear and anti-fatigue performances of different wheel-rail material matchings were discussed. Furthermore, the critical value of sand deposition density for relieving the wear and damage of wheel and rail was also suggested based on this experimental investigation.

## 2. Experimental details

In this work, all the experiments were conducted on a twin-disc machine with a sand feeder, as shown in Fig. 2. Two cylindrical specimens were mounted on two shafts (i.e., mobile shaft and fixed shaft), which were individually driven by two alternating current motors with a power of 33 kW. The sliding table equipped with a mobile shaft can be pushed or pulled by the hydraulic cylinder to achieving the loading and unloading of normal force. The maximum rotation speed of specimens can reach 1200 rpm and the maximum normal force can reach 75 kN. During the tests, the rotation speed of specimens, torque, normal force and the number of cycles can be collected by the data acquisition system, and the real-time friction coefficient can also be calculated based on the collected data. The slip ratio of the wheel and rail specimens can be realized by controlling the rotation speed of altering current motors, which can be calculated by the following Equation (1):

$$\gamma = \frac{2(n_{\text{rail}} d_{\text{rail}} - n_{\text{wheel}} d_{\text{wheel}})}{n_{\text{rail}} d_{\text{rail}} - n_{\text{wheel}} d_{\text{wheel}}} \times 100 \quad (1)$$

where $\gamma$ is the slip ratio of specimens; $n_{\text{rail}}$ and $n_{\text{wheel}}$ are the rotation speed of rail and wheel specimens respectively, r/min; $d_{\text{rail}}$ and $d_{\text{wheel}}$ are the diameters of rail and wheel specimens respectively, m. The sand deposition density applied on specimen surface can be controlled by the sand feeder with different sand feed rate, which can be calculated by the following Equation (2):

$$\rho_D = \frac{f}{\pi d n W} \quad (2)$$

where $\rho_D$ is the sand deposition density, g/m$^2$; $f$ is the sand feed rate, g/min; $d$ is the diameter of specimen, m; $n$ is the rotation speed of faster specimen, r/min; $W$ is the wear bandwidth of specimens, m. In addition, due to the horizontal contact of wheel and rail specimens, the control of rolling direction and the gravitational action of sand (Fig. 2), all sand particles would be sucked into the wheel-rail interface and crushed.

In all tests, the shape and dimension of wheel and rail specimens were identical. The diameter and width of specimens were 60 mm and 15 mm, respectively. The wheel specimens and rail specimens were machined from the wheel tread and rail head, respectively. Test parameters are listed in Table 1. Four types of wheel-rail material matchings were studied in this work, which consisted of two Chinese wheel steels (CW1 and CW2), two European wheel steels (EW1 and EW2), one Chinese rail steel (U75V) and one European rail steel (900A). The tests of each wheel-rail material matching were performed under six levels of sand deposition density, i.e., 0, 0.1, 0.2, 0.4, 1 and 3 g/m$^2$, which based on the typical values of sand mass per unit area by collecting and weighing the sand deposited on the rail top area in desert environments. It should be noted that a commercial sand with the similar composition to the real desert sand in the previous work [15] was used in these tests due to the some limitations of test condition in this work. The average size of the sand was about 300 μm and the morphology of sand particles was shown in Fig. 3. All the tests were performed under the slip ratio of 2 % and Hertzian contact pressure of 1100 MPa. The total number of cycles was 40,000. The rotation speed of rail specimens was about 500 r/min, which was slightly faster than that of wheel specimen (about 490 r/min).

The chemical composition and hardness of wheel and rail steels are listed in Table 2. It shows that the hardness of these steels was similar although there were some differences in carbon content. Furthermore, the matrix microstructures of the wheel and rail steels are shown in Fig. 4. It presented that the microstructure of wheel and rail steels


**Fig. 1.** Windblown sand hazard: (a) track buried by sand [8]; (b) wear and damage of rail [9]; (c) hollow wear and damage of wheel [3,6].

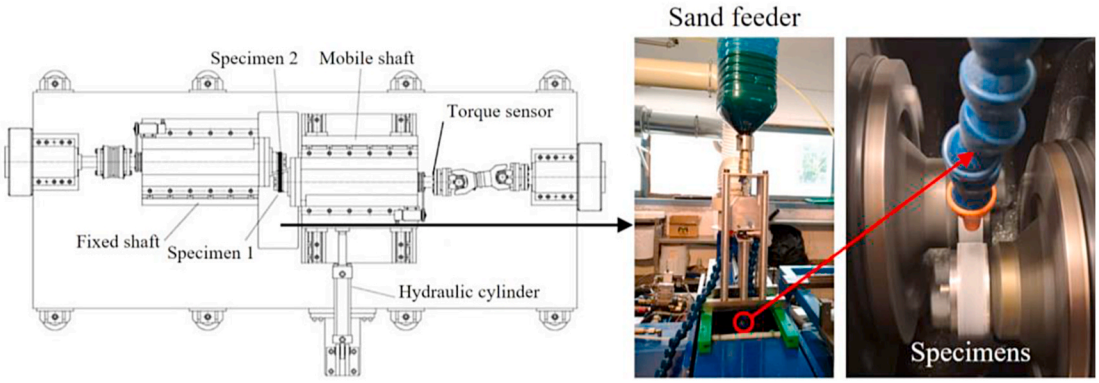


**Fig. 2.** Test machine [20].

**Table 1**
Test parameters.

| Wheel | Rail | Sand deposition density (g/m$^2$) | Slip ratio (%) | Contact pressure (MPa) | Speed of rail specimen (rpm) | Cycles |
|---|---|---|---|---|---|---|
| CW1<br>CW2<br>EW1<br>EW2 | U75V<br><br>900A | 0, 0.1, 0.2, 0.4, 1, 3 | 2 | 1100 | 500 | 40,000 |


**Fig. 3.** Morphology of sand particles.

**Table 2**
Chemical composition and hardness of wheel and rail steels.

| Wheel/rail steel | | Chemical composition (wt%) | | | | | Hardness ($HV_{0.2}$) |
|---|---|---|---|---|---|---|---|
| | | C | Si | Mn | P | S | |
| Wheel | CW1 | 0.60 | 0.27 | 0.75 | 0.035 | 0.040 | 311 |
| | CW2 | 0.54 | 0.68 | 0.70 | 0.0047 | 0.0013 | 313 |
| | EW1 | 0.52 | 0.37 | 0.74 | ≤0.020 | ≤0.015 | 302 |
| | EW2 | 0.50 | 0.89 | 0.93 | | | 312 |
| Rail | U75V | 0.76 | 0.75 | 0.88 | ≤0.030 | ≤0.030 | 305 |
| | 900A | 0.71 | 0.27 | 1.07 | 0.006 | 0.010 | 302 |

(Fig. 4a–f) consisted mainly of pearlite and proeutectoid ferrite. The area percentage of proeutectoid ferrite in wheel and rail steels is shown in Fig. 4g. Combined with the carbon content in Table 2, the area percentage of proeutectoid ferrite in wheel steel increased with the decrease in carbon content. Additionally, the content of proeutectoid ferrite in 900A rail steel was higher than that in U75V rail steel, whereas its value was far lower than that of wheel steels.

Before and after the tests, the specimens were cleaned by an ultrasonic cleaner with anhydrous ethanol and weighed by an electronic balance with high precision of 0.001 g. The wear rate of specimens was calculated based on the mass loss of specimens before and after tests. After the tests, a small piece with the dimensions of 15 mm × 10 mm × 5 mm was cut from each worn specimen to determine the surface and subsurface damages, as shown in Fig. 5. The surface and subsurface damages were detected by a laser confocal microscope (LSCM, OLS5000-SAF, Japan), an ultra-depth of field 3D microscopic system (KEYENCE VHX-5000, Japan), and a scanning electron microscope (SEM, TESCAN MIRA LMS, Czech Republic). The oxides on worn surface were analyzed by a laser confocal Raman spectrometer (HV Evolution, Japan) and an X-ray photoelectron spectrometer (XPS, ESCALAB 250Xi, America). The hardness of matrix and worn surface was determined by a Vickers hardness instrument (HV-1000, China). The microstructure of specimens was analyzed by a Hitachi S-3400 N SEM equipped with an HKL-EBSD (Electron Back Scatter Diffraction) system.

## 3. Results

### 3.1. Adhesion coefficient

Fig. 6 shows the relationship between adhesion coefficient and sand deposition density. It can be seen that with the increase in sand deposition density, adhesion coefficient exhibited an overall decline trend for different wheel-rail material matchings. The significant decline trend mainly appeared in the range of 0~0.2 g/m$^2$. In addition, some fluctuations could also be observed during 0.2–1 g/m$^2$. A reasonable explanation would be given in the discussion section based on the later microanalysis results.

### 3.2. Wear rate

Fig. 7 presents the variation trend of wear rate with sand deposition density. It can be seen from Fig. 7a that with the increase in sand deposition density, the wear rate of CW1 and CW2 Chinese wheel steels first dramatically decreased and then increased, and finally decreased again. The minimum wear rate occurred at around 0.1–0.2 g/m$^2$, and the maximum wear rate occurred at 1.0 g/m$^2$. However, the wear rate of EW1 and EW2 European wheel steels first increased and then decreased. The maximum wear rate of EW1 and EW2 occurred at around 0.2 g/m$^2$ and 1 g/m$^2$, respectively.

Fig. 7b shows that with the increase in sand deposition density, the variation trends of U75V Chinese rail steel wear rate against CW1 and CW2 wheel steels were quite similar to that of corresponding wheel steel. However, the wear rate of 900A rail steel against EW1 first dramatically declined and then increased, and finally kept relatively stable. The minimum wear rate of 900A rail steel against EW1 occurred

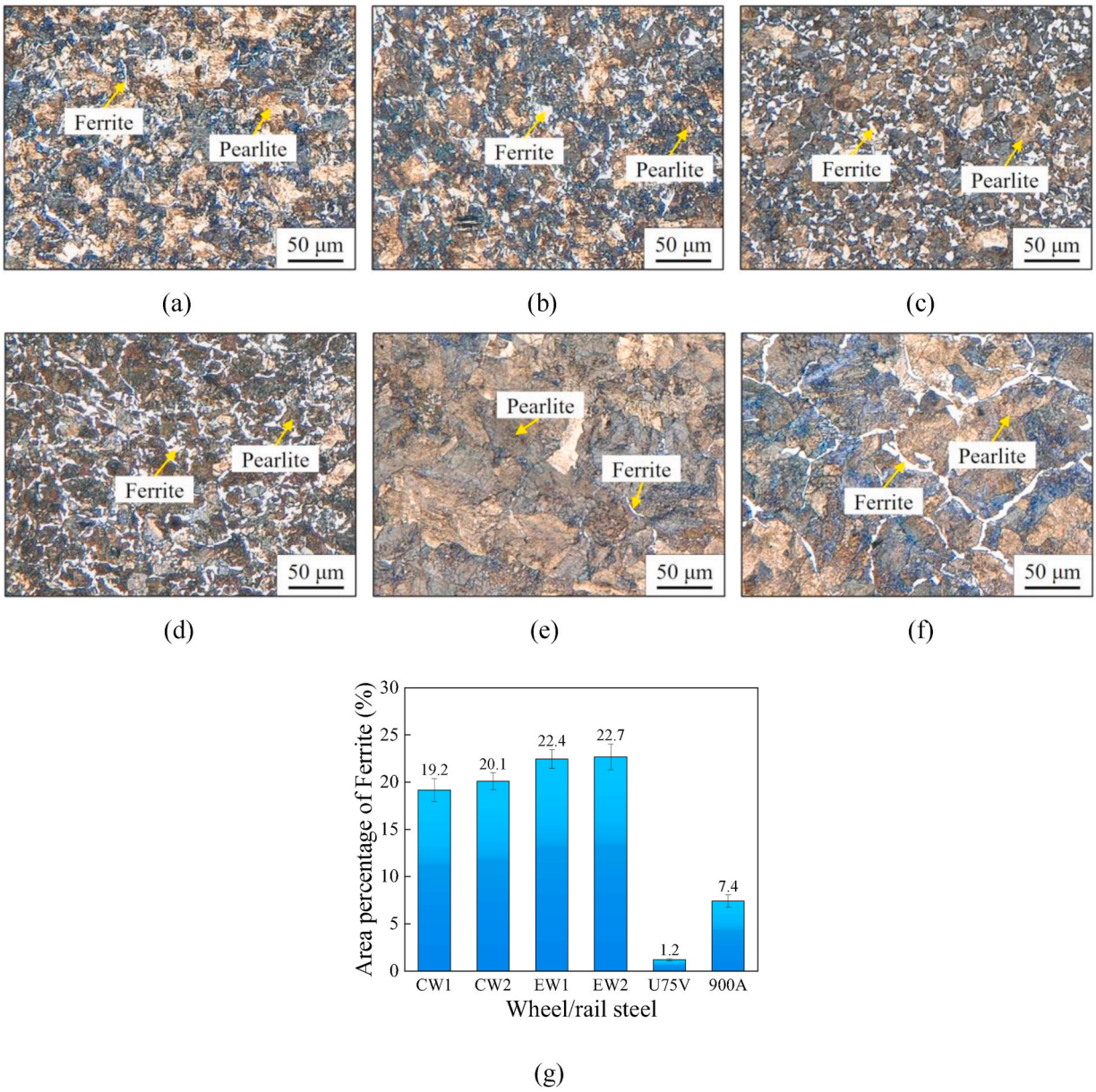


**Fig. 4.** Matrix microstructure of wheel and rail steels: (a) CW1; (b) CW2; (c) EW1; (d) EW2; (e) U75V; (f) 900A; (g) area percentage of ferrite.

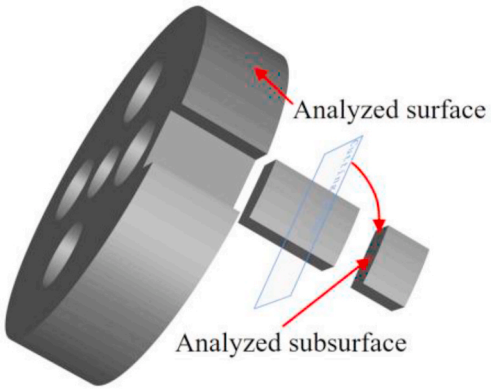


**Fig. 5.** Microanalysis positions of specimens after tests.

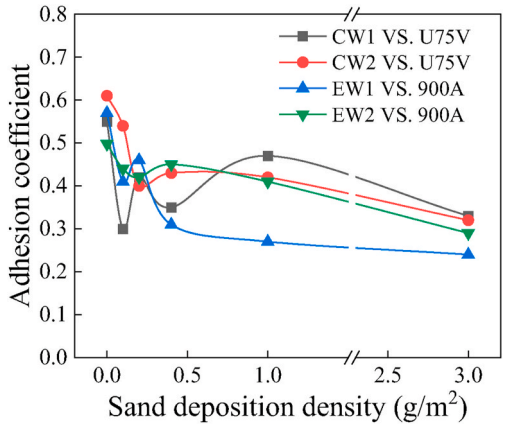


**Fig. 6.** Adhesion coefficient vs. sand deposition density for different wheel-rail material matchings.

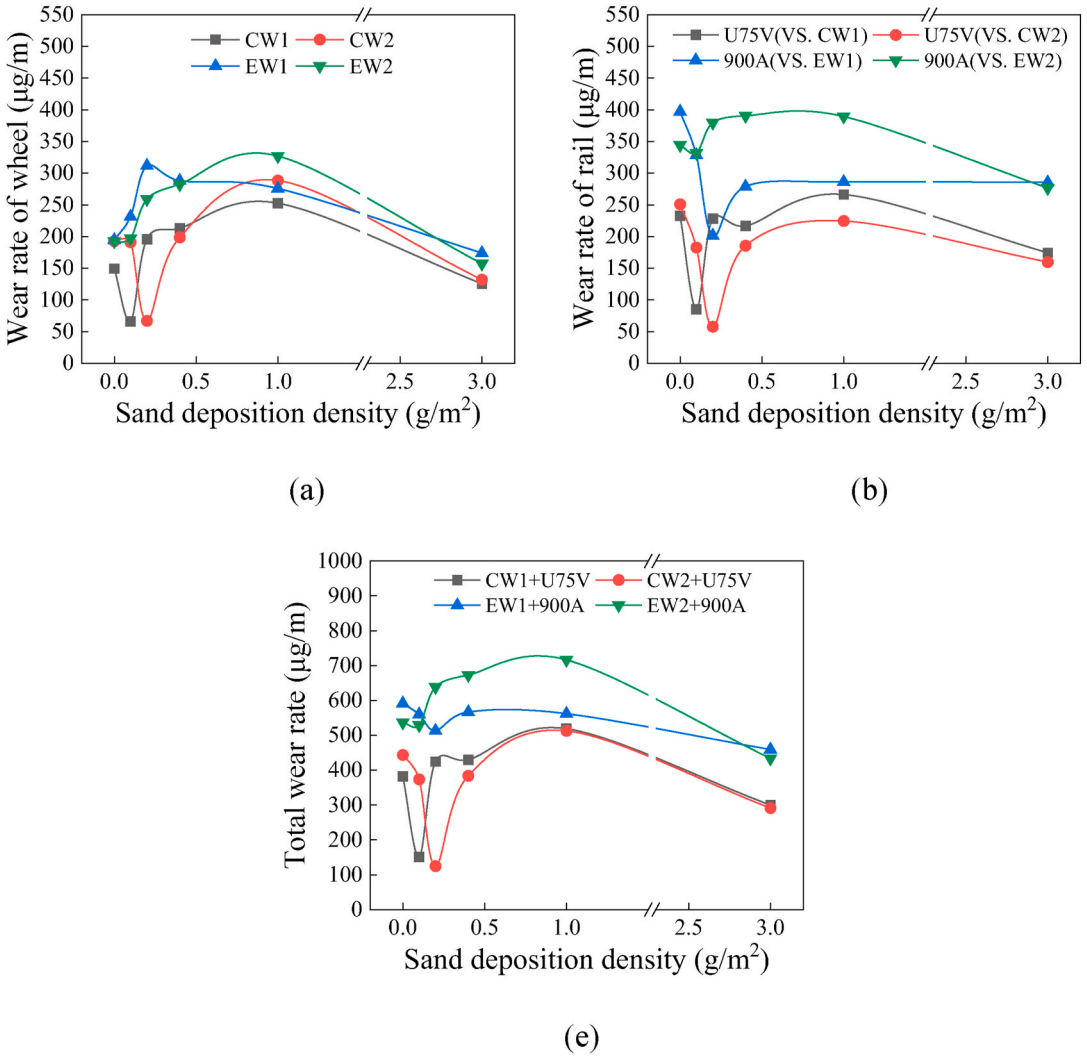


**Fig. 7.** Wear rate vs. sand deposition density: (a) wheel; (b) rail; (c) total (wheel + rail).

at 0.2 g/m$^2$. However, the wear rate of 900A rail steel against EW2 first declined and then increased, and finally decreased again. Additionally, the wear rate of European rail steels was higher than that of Chinese rail steels, which might be caused by the higher carbon content of Chinese rail steels.

Fig. 7c presents that the total wear rate of wheel and rail for different

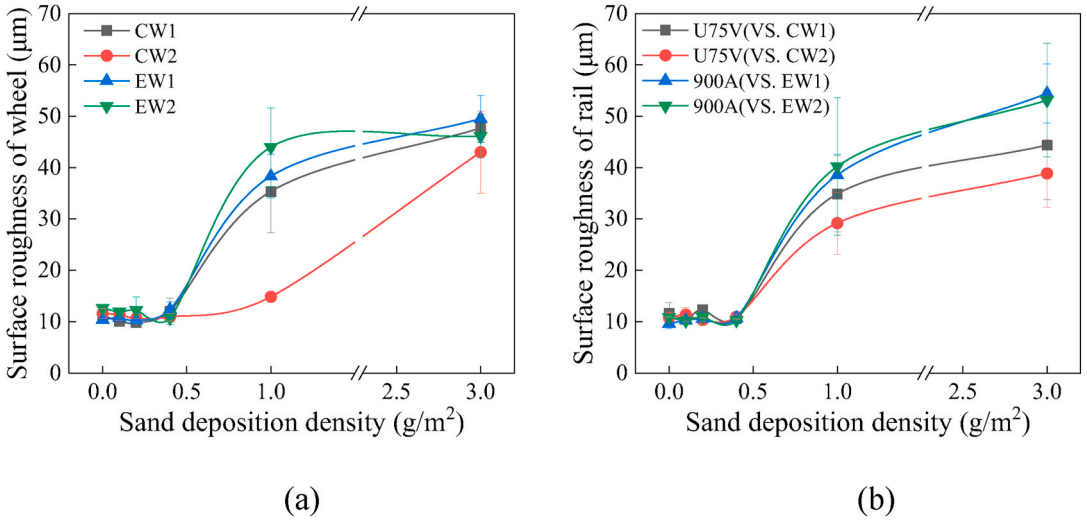


**Fig. 8.** Surface roughness vs. sand deposition density: (a) wheel; (b) rail.

wheel-rail material matchings exhibited a similar variation trend with sand deposition density. A minimum wear rate generally appeared in the range of 0.1–0.2 g/m$^2$. The maximum wear rate mainly appeared at about 1.0 g/m$^2$ except for [EW1-900A] matching. Furthermore, Chinese wheel-rail material matching exhibited better anti-wear performance compared with European wheel-rail material matching.

### 3.3. Surface roughness and hardness

Fig. 8 shows the results of surface roughness after tests under different sand deposition densities. It can be seen that the surface roughness of wheel (Fig. 8a) and rail (Fig. 8b) had a similar variation trend with sand deposition density. The surface roughness kept stable and the value was about 10 μm in the range of 0~0.4 g/m$^2$, whereas it increased sharply first and then slowly when sand deposition density exceeded 0.4 g/m$^2$. In addition, the surface roughness of European wheel and rail steels was generally higher than that of Chinese wheel and rail steels when sand deposition density exceeded 1 g/m$^2$.

In order to compare the surface hardness of wheel and rail for different wheel-rail material matchings, the hardness was determined at a distance of 45 μm from the surface because the worn surface was too rough to measure the hardness accurately, as shown in Fig. 9a. The surface hardness of wheel and rail varying with sand deposition density was presented in Fig. 9b and c, respectively. It is clear from Fig. 9b that as increasing the sand deposition density, the surface hardness of CW1 increased first, peaking at 0.4 g/m$^2$, and then decreased slowly. The surface hardness of CW2 presented an increasing trend. However, the surface hardness of EW1 and EW2 had a similar variation trend of decreasing first and then increasing, and the minimum hardness appeared in the range of 0.1–0.2 g/m$^2$. Fig. 9c shows that the variation trend of rail surface hardness with sand deposition density was similar to that of wheel surface hardness (Fig. 9b).

### 3.4. Surface damage

The optical images of wheel surface damage under different sand deposition densities are presented in Table 3. Only the surface damage of wheel was illustrated here because the surface damage of the corresponding rail was quite similar to that of wheel. It can be observed that there was no significant difference in surface damage morphology for different wheel/rail steels under the same sand deposition density. Under the condition without sand (0 g/m$^2$), obvious fatigue crack was the main surface damage feature. When the sand deposition density exceeded 0.2 g/m$^2$, it was difficult to observe the obvious fatigue crack on the damaged surface, whereas spotted oxide was always generated on the surface. When the sand deposition density exceeded 1 g/m$^2$, grooves would be formed on the surface, and the width and depth of grooves increased with the increase in sand deposition density. It was consistent with the results of surface roughness in Fig. 8. Therefore, it can also be concluded that the surface damage deteriorated severely when sand deposition density exceeded a certain level.

In order to analyze the surface damage further, the SEM images of surface damage at different sand deposition densities were presented in Fig. 10. It shows that as the sand deposition density increased, the surface fatigue cracks were gradually reduced, and the sand fragments embedded on the surface were more easily observed. In addition, with the increase in sand deposition density, the oxides distribution density increased first, peaking at around 0.2 g/m$^2$ (Fig. 10b), and then decreased. It can also be concluded that as increasing the sand deposition density, the oxidative wear increased sharply first and then decreased slowly, whereas the fatigue wear decreased consistently. Furthermore, the abrasive wear increased due to the increase in the sand

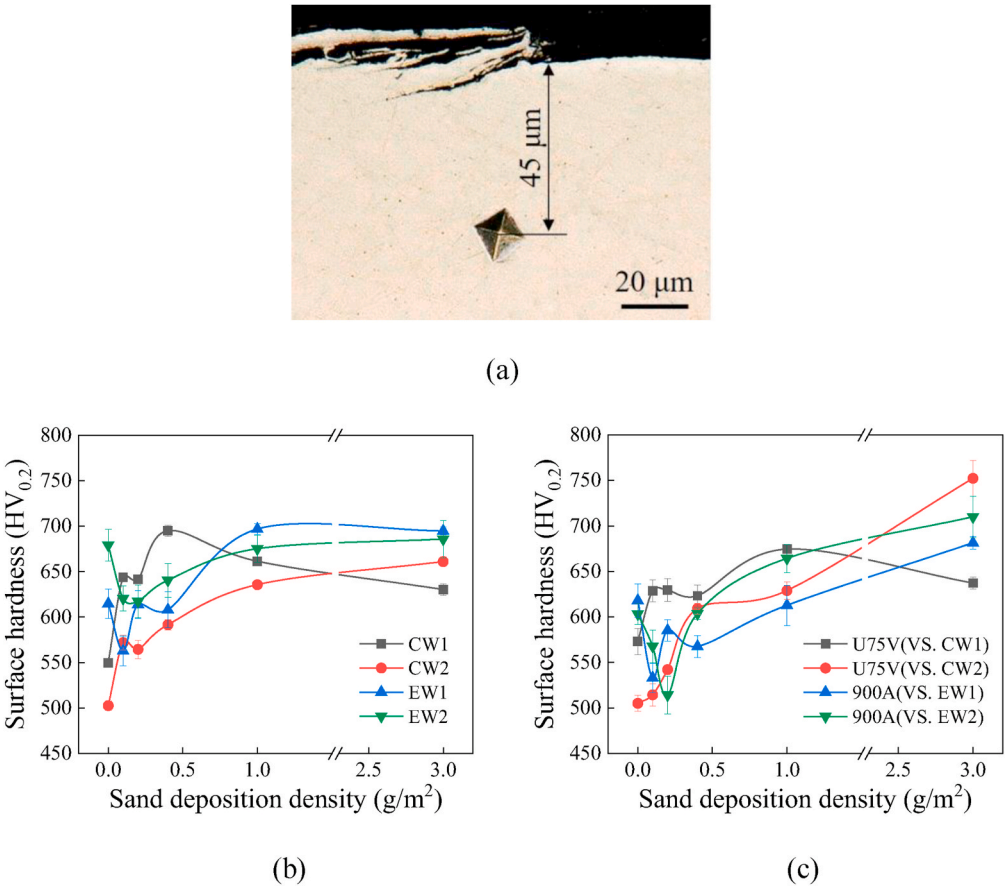


**Fig. 9.** Surface hardness vs. sand deposition density: (a) position of hardness measuring; (b) wheel surface hardness; (c) rail surface hardness.

**Table 3**
Optical images of surface damage for wheel and rail steels under different sand deposition densities.

| | CW1 | CW2 | EW1 | EW2 |
|---|---|---|---|---|
| 0 g/m$^2$ | 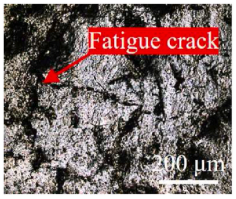  | 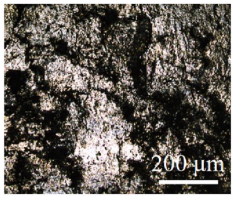  |   | 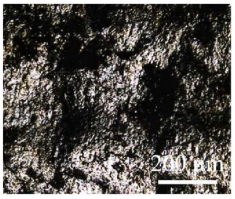  |
| 0.2 g/m$^2$ | 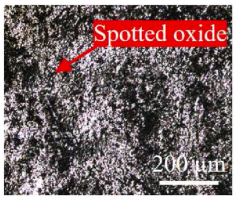  | 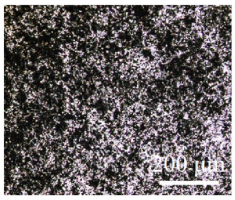  | 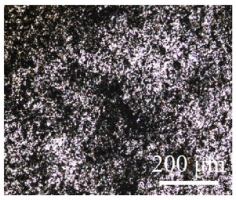  | 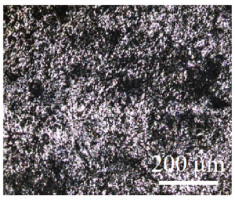  |
| 1 g/m$^2$ | 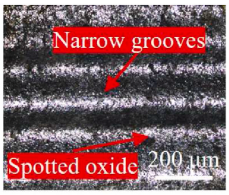  | 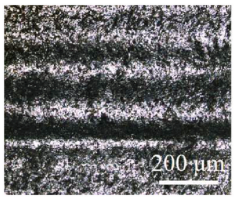  | 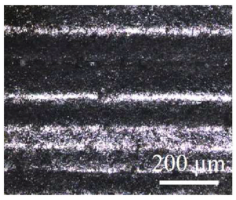  | 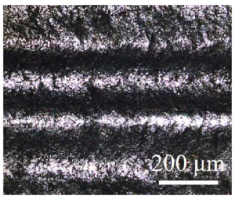  |
| 3 g/m$^2$ | 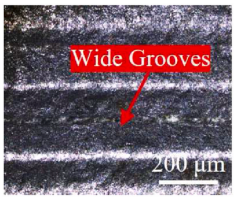  | 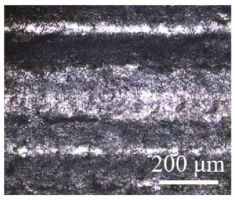  | 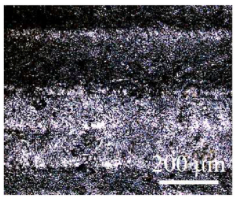  | 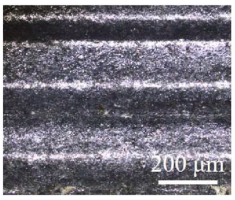  |

particles and its fragments.

The method of Raman spectra was applied to analyze the oxides on the damaged surface, and the results were presented in Fig. 11. It can be seen that the oxides on the damaged surface were composed of $Fe_3O_4$ and α-$Fe_2O_3$ [21]. The main content was $Fe_3O_4$ because the intensity of $Fe_3O_4$ peak was significantly stronger than that of α-$Fe_2O_3$ peak.

Furthermore, another method of XPS was also applied to analyze the content of oxides on damaged surface, as shown in Fig. 12. It can be seen from Fig. 12a that there were two peaks located at about 724.6 eV and 710 eV, representing Fe $2p_{1/2}$ and Fe $2p_{3/2}$ respectively [22,23]. Fe $2p_{3/2}$ peak could be used to analyze the content of iron oxides here because the intensity of Fe $2p_{3/2}$ peak was significantly stronger than that of Fe $2p_{1/2}$. The peak of Fe $2p_{3/2}$ could be decomposed into peaks of Fe, $Fe^{2+}$ and $Fe^{3+}$, as shown in Fig. 12b [22]. The binding energy, FWHM, percentage of $Fe^{2+}$ and $Fe^{3+}$, and ratio of $Fe^{3+}/Fe^{2+}$ are listed in Table 4. The ratio of $Fe^{3+}/Fe^{2+}$ in the oxides was 2.268. Based on the analysis result of the above Raman spectra (Fig. 11), the oxides were composed of $Fe_3O_4$ and α-$Fe_2O_3$. The ratio of $Fe^{3+}/Fe^{2+}$ in $Fe_3O_4$ and α-$Fe_2O_3$ were 2 and $+\infty$, respectively. Therefore, the ratio of $Fe^{3+}/Fe^{2+}$ in the oxides on the damaged surface was close to that of $Fe_3O_4$, i.e., the main content of oxides was $Fe_3O_4$. It also indicated that the results of XPS analysis were consistent with those of Raman spectrum analysis.

Some previous studies reported that the oxides would form on the wheel and rail surfaces under the low contact stress conditions [24–27]. Similarly, the formation of oxides in this work was also caused by the low contact stress because the existence of sand particles and its fragments reduced the actual contact stress in direct contact area of wheel and rail materials. In addition, the oxide of $Fe_3O_4$ could act as an important lubricant for reducing friction and wear [22,24,28], which might also be the main reason for the sharp decrease of adhesion coefficient (Fig. 6) and wheel/rail wear rate (Fig. 7) at the sand deposition density of 0~0.2 g/m$^2$.

### 3.5. Subsurface damage

Fig. 13 shows the plastic deformation morphologies of longitudinal section and cross section under the conditions of low and high sand deposition densities. It can be seen from Fig. 13 a and c that plastic deformation line was inclined upward in the longitudinal section due to the combined action of shear force and normal force. However, in the cross section (Fig. 13b and d), the plastic deformation line was parallel to the surface attributing to the extrusion action of normal force. Furthermore, under the condition of high sand deposition density (Fig. 13d), obvious wavy morphology could be observed on the cross section, which was consistent with the grooves observed in Table 3.

According to the measuring method in Fig. 13a, the plastic deformation depth of different wheel and rail steels at all conditions was measured and the results were presented in Fig. 14. It can be seen from Fig. 14a that the variation trend of plastic deformation depth for different wheel steels was different when sand deposition density was in the range of 0~0.4 g/m$^2$, whereas it presented an increasing trend when sand deposition density exceeded 0.4 g/m$^2$. There was almost a minimum plastic deformation depth at about 0.1–0.2 g/m$^2$ for all wheel steels, which might be attributed to the formation of oxides. Fig. 14b shows that the variation trend of plastic deformation depth for different rail steels was generally similar to that of corresponding wheel steels. In addition, a minimum plastic deformation depth generally occurred at about 0.1–0.2 g/m$^2$ for all rail steels.

In order to better evaluate the subsurface fatigue damage, the crack depth under all conditions was determined according to the method

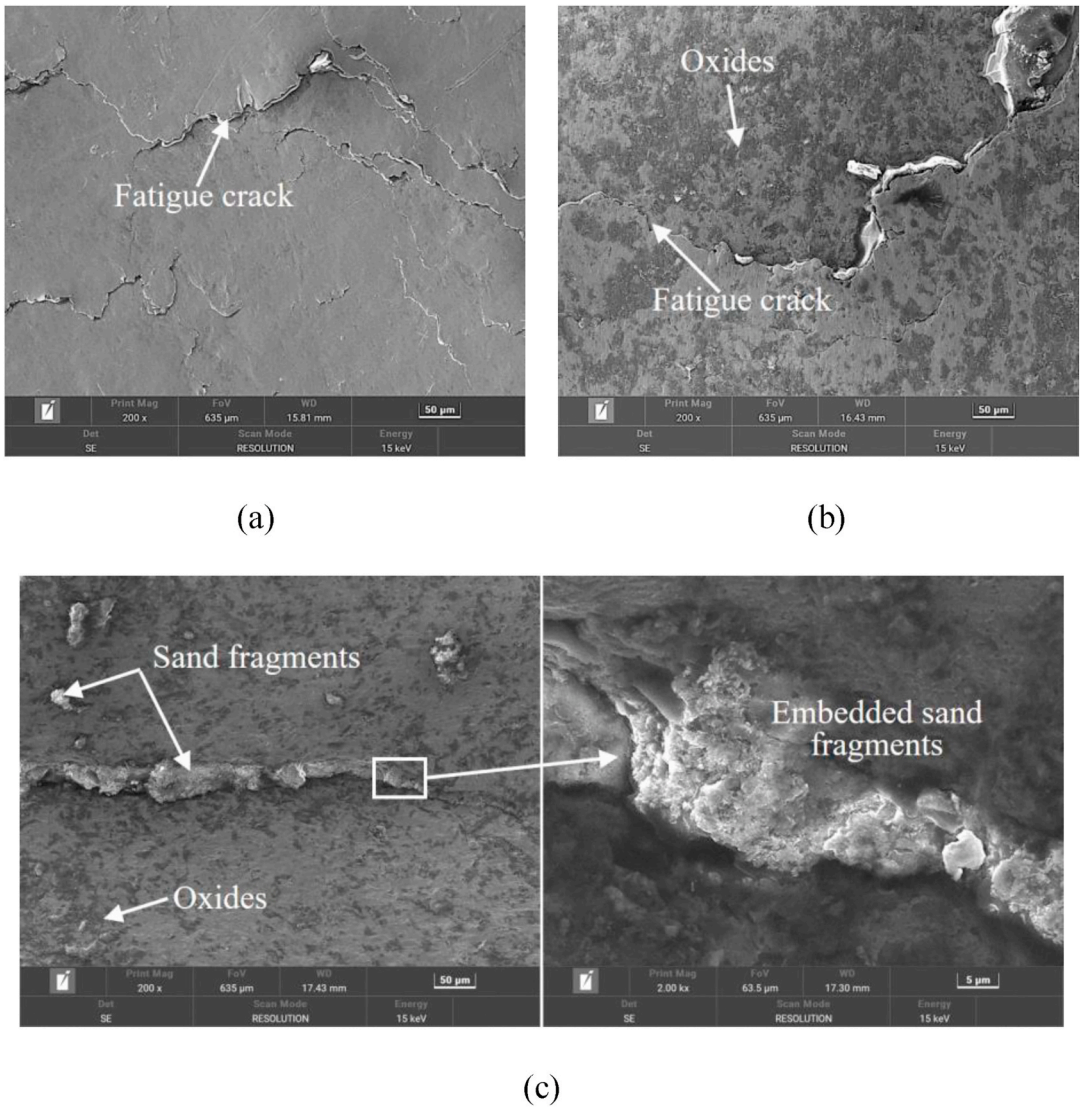


**Fig. 10.** SEM images of surface damage at different sand deposition densities: (a) 0 g/m$^2$; (b) 0.2 g/m$^2$; (c) 3 g/m$^2$.

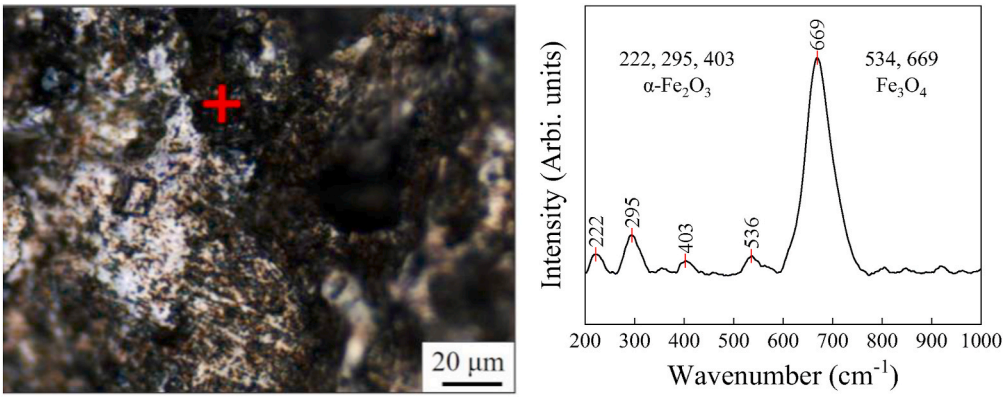


**Fig. 11.** Raman spectra analysis of oxides on damaged surface (Fig. 10b) at sand deposition density 0.2 g/m$^2$.

illustrated in Fig. 15d. The results of crack depth of wheel and rail were presented in Fig. 15a and b, respectively. It can be observed from Fig. 15a that the average crack depth of CW2 and EW1 wheel steels presented a similar variation trend with sand deposition density, i.e., decreased first, reaching a minimum value, and then increased. However, CW1 and EW2 wheel steels presented a slow downward trend. CW1 wheel steel exhibited the best anti-fatigue performance among these four types of wheel steels. Fig. 15b shows that the average crack depth of all rail steels generally presented an upward trend with sand deposition density. The anti-fatigue performance of U75V rail steel was

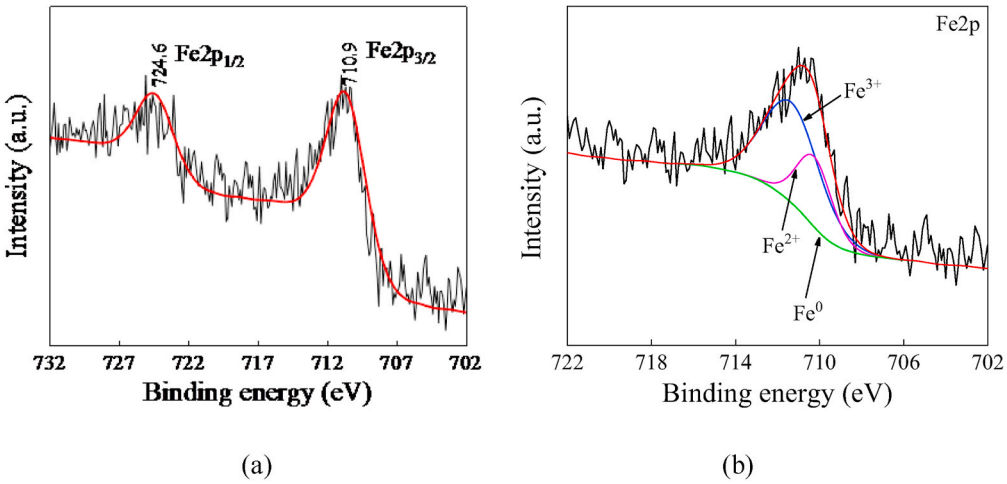


**Fig. 12.** XPS analysis of damaged surface at sand deposition density 0.2 g/m$^2$ (Fig. 10b): (a) Fe 2p spectra; (b) fitted peaks of Fe 2p$_{3/2}$ spectra.

**Table 4**
Binding energy, FWHM, percentage of $Fe^{2+}$ and $Fe^{3+}$, and ratio of $Fe^{3+}/Fe^{2+}$ (Fig. 12b).

| | Binding energy (eV) | FWHM (eV) | Percentage (%) | Ratio of $Fe^{3+}/Fe^{2+}$ |
|---|---|---|---|---|
| $Fe^{2+}$ | 710.24 | 2.04 | 30.6 | 2.268 |
| $Fe^{3+}$ | 711.33 | 3.28 | 69.4 | |

better than that of 900A rail steel under the condition of high sand deposition density. Furthermore, it can be concluded from Fig. 15a and b that the crack depth was almost less than 30 μm for all wheel and rail steels when the sand deposition density was lower than 1 g/m$^2$, whereas the crack depth of rail exceeded 50 μm when the sand deposition density reached 3 g/m$^2$. In addition, the morphologies of crack with small depth and large depth were shown in Fig. 15c and d, respectively. Fig. 15d shows that the crack with large depth was formed by the superposition of multi-layer thin cracks, which might be attributed to the rolling-sliding effect of a large number of sand particles at high sand

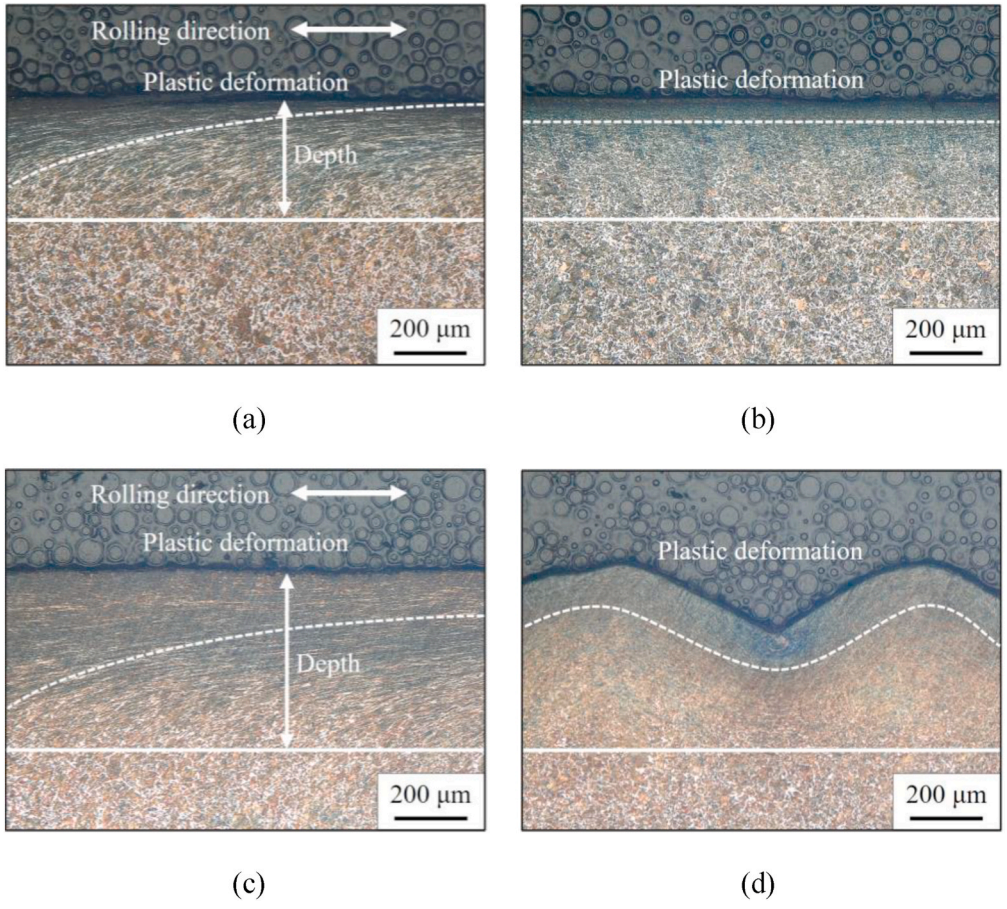


**Fig. 13.** Plastic deformation: (a) longitudinal section at 0.2 g/m$^2$; (b) cross section at 0.2 g/m$^2$; (c) longitudinal section at 3 g/m$^2$; (d) cross section at 3 g/m$^2$.

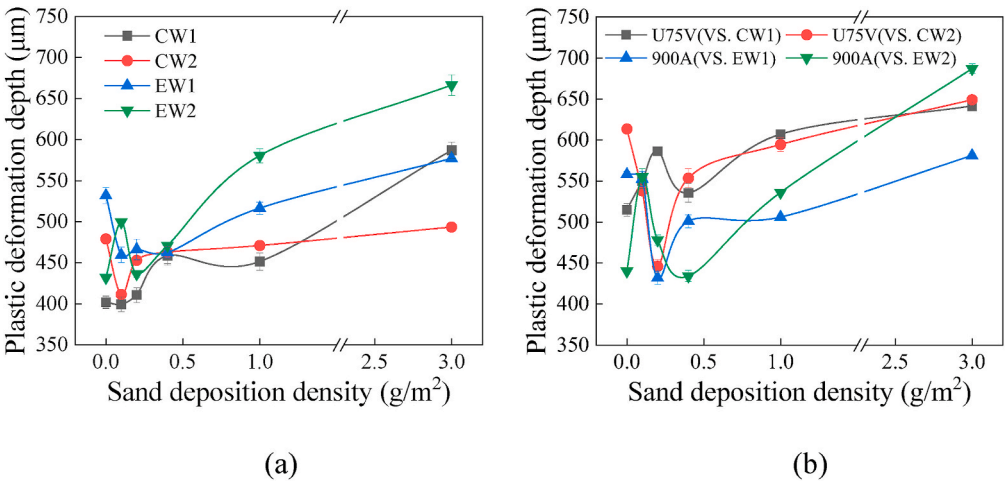


**Fig. 14.** Plastic deformation depth vs. sand deposition density: (a) wheel; (b) rail.

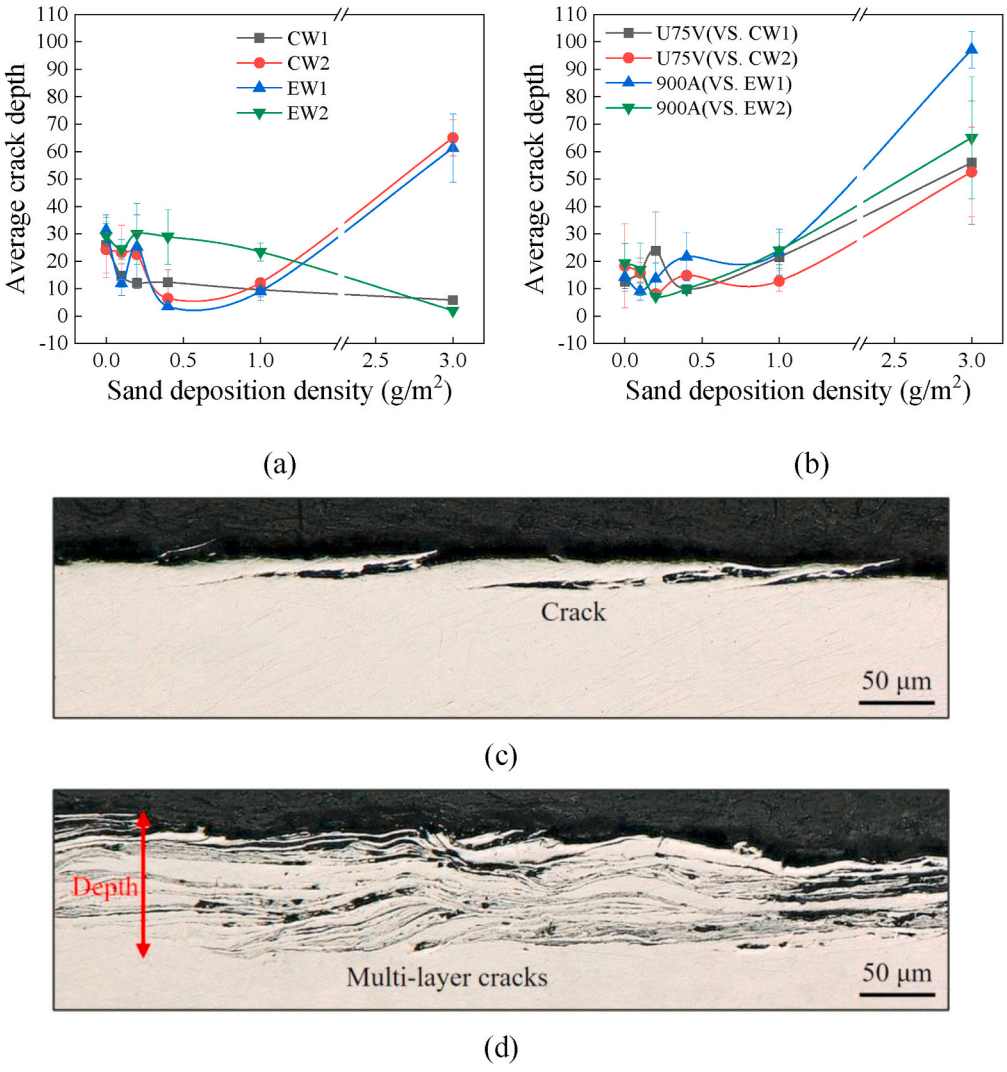


**Fig. 15.** Crack depth and morphology: (a) average crack depth of wheel vs. sand deposition density; (b) average crack depth of rail vs. sand deposition density; (c) morphology of crack with small depth; (d) morphology of crack with large depth at high sand deposition density (3 g/m$^2$).

deposition density.

Furthermore, the top layer and matrix microstructures of longitudinal section in the condition of high sand deposition density (3 g/m$^2$) were analyzed using EBSD method, as shown in Fig. 16. The inverse pole figure (IPF), grain boundary map, recrystallization map and pole figure of top layer were respectively shown in Fig. 16b, c, d, and h, whereas

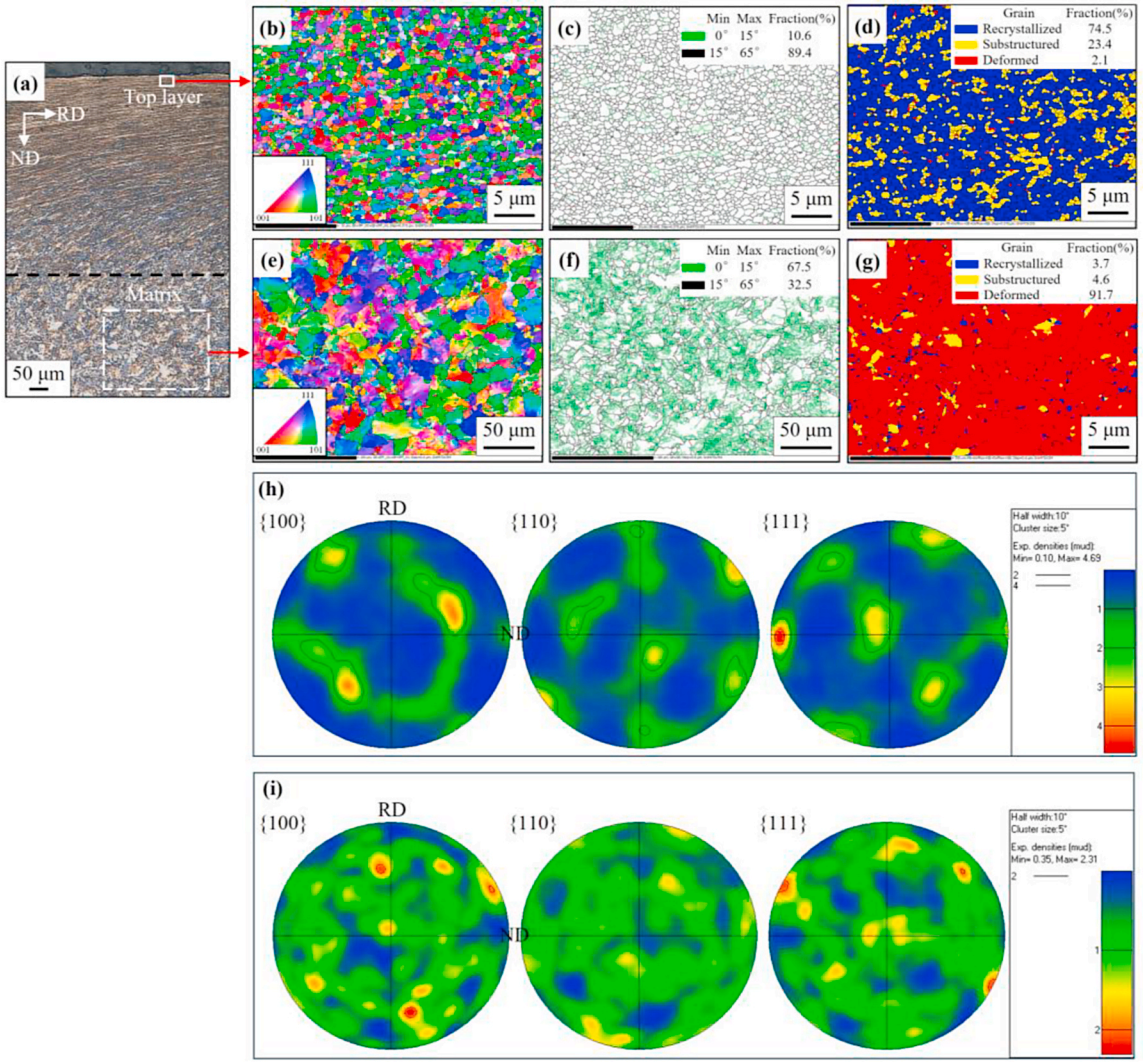


**Fig. 16.** EBSD analysis of wheel steel at high sand deposition density (3 g/m$^2$): (a) analyzed regions (optical image); (b) and (e) inverse pole figure (IPF); (c) and (f) grain boundary map; (d) and (g) recrystallization map; (h) and (i) pole figure (PF). Top layer: (b), (c), (d), and (h); Matrix: (e), (f), (g) and (i). RD and ND represent rolling direction and normal direction, respectively.

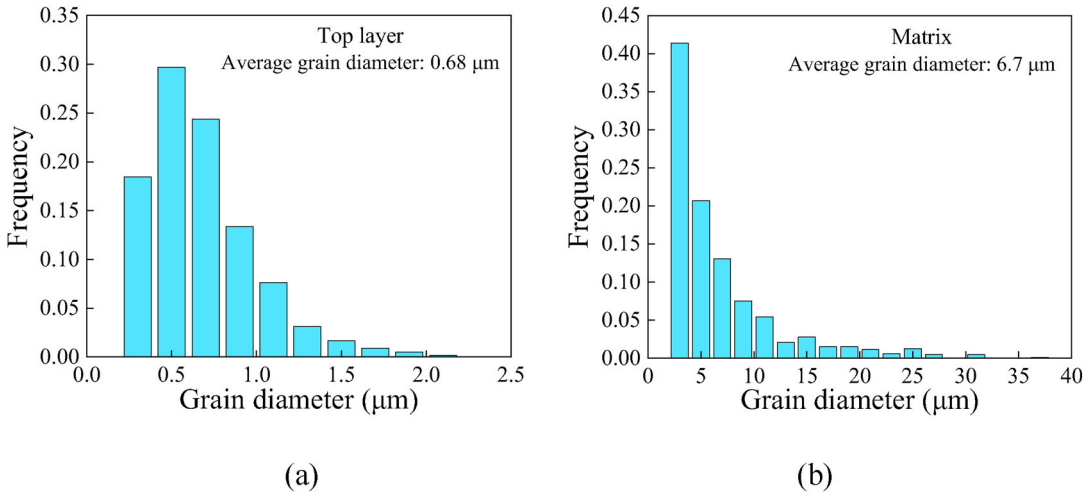


**Fig. 17.** Grain diameter distribution corresponding to Fig. 16b and e: (a) top layer; (b) matrix.

those of matrix were respectively shown in Fig. 16e, f, g, and i.

Fig. 16a shows that the microstructure of top layer was fibrous and almost parallel to the rolling direction attributing to the strong shearing stress, whereas the microstructure of matrix was randomly distributed. Fig. 16b and e shows that the microstructure of top layer was composed of a great many of ultra-fine grains, whereas the microstructure of matrix was mainly composed of large diameter grains. In addition, the grain diameter distribution of top layer and matrix were illustrated in Fig. 17a and b, respectively. In the top layer, the frequency of grains with a diameter of 0.5 μm was the highest and its value was about 30 %, whereas in the matrix, the frequency of grains with a diameter of 3 μm was the highest and its value was about 41 %. It is known that the size of the grain determines the properties of the metal materials, e.g., smaller grain size can improve the hardness, tensile strength and ductility of metal material. Therefore, the above results also indicated that the material properties of the top layer were improved evidently under the condition of rolling contact, e.g., the hardness of the top layer was much higher than that of the matrix (Fig. 9b and c).

Fig. 16c and f shows that the microstructure in the top layer was mainly distributed with high-angle grain boundaries (HAGBs, 15°~65°), whereas the microstructure in the matrix was mainly distributed with low-angle grain boundaries (LAGBs, 0°~15°). Furthermore, the misorientation angle distributions in the top layer and matrix were presented in Fig. 18. In the top layer, the misorientation angle was distributed over a wide range and the frequency of different misorientation angles was relatively uniform. The frequency of misorientation angle about 45° was the highest and its value was only about 3 %. However, in the matrix, the distribution of misorientation angle was relatively concentrated. The frequency of misorientation angle about 2° was the highest and its value was about 23 %. The average misorientation angle in the top layer microstructure was significantly higher than that in the matrix microstructure. Since the grain boundary refers to the outside area of a grain that separates it from the other grains. Meanwhile, according to the level of misorientation angle between adjacent grains, the grain boundary is classified into HAGBs (15°~65°) and LAGBs (0°~15°). Therefore, the above results also indicated that the misorientation angle between adjacent grains of the top layer increased significantly under the condition of rolling contact.

Fig. 16d and g shows that the top layer microstructure was mainly composed of recrystallized grains, whereas the matrix microstructure was mainly composed of deformed grains. Due to the rolling and heat treatment of these wheel materials in the manufacturing process, a large number of dislocations were generated in the deformed grains, and some broken grains were also formed, which resulted in the formation of LAGBs with high proportion in the matrix microstructure. Meanwhile, it is known that the recrystallization growth of grains would result in the reduction of LAGBs and the increase of HAGBs, and finally formed recrystallized grains. Therefore, the results of Fig. 16d and g could provide a strong explanation for the results of Fig. 16c and f.

Fig. 16h presents that the top layer microstructure had a high polar density with the maximum intensity of 4.69, indicating that the top layer microstructure had a preferential orientation. The main reason was that under the action of normal stress and shear stress, the grains were deformed and slid along the sliding direction on the sliding plane. However, the crystal orientation of matrix exhibited significant randomness, as shown in Fig. 16i.

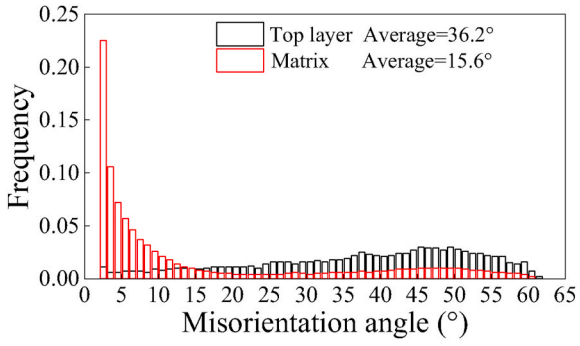


**Fig. 18.** Misorientation angle distribution of grain boundary corresponding to Fig. 16c and f.

Based on the analysis of Figs. 16–18, it can be concluded that under the action of normal stress and shear stress, the matrix microstructure with large size deformed grains, low angle grain boundaries and random textures gradually evolved into the top microstructure with ultra-fine recrystallized grains, high angle grain boundaries and preferred orientation textures. The results observed in this work were consistent with those reported in other previous studies [29–31]. The main reason was that the action of normal stress and shear stress made the coarse grains break into sub-grains first, and then further refined and generated continuous dynamic recrystallization (cDRX), and finally formed ultra-fine grains with preferred orientation textures.

Similarly, the EBSD analysis method was also applied to analyze the microstructures of CW1, CW2, EW1 and EW2 wheel steels, and the statistical results were illustrated in Fig. 19. It can be seen from Fig. 19a that the average diameter in the top layer was about 0.65 μm for all wheel steels. The matrix grain diameters of European wheel steels (EW1 and EW2) were slightly higher than those of Chinese wheel steels (CW1 and CW2). Furthermore, the grain diameter in the matrix was generally 10 times of that in the top layer for all wheel steels, which was also the main reason for the surface hardness (Fig. 9b) after tests was significantly higher than that of matrix.

Fig. 19b shows that the average misorientation angle in the top layer was about 37° for all wheel steels. However, in the matrix, there was a relatively large difference in misorientation angle for different wheel steels, and the average misorientation angle could be ranked as: CW2 > EW1 > EW2 > CW1. Fig. 19c shows that the maximum intensity of the pole figure in the top layer was about 4.7 for all wheel steels, which indicated the microstructure in the top layer exhibited the similar preferred orientation. However, in the matrix, there was a relatively large difference in the maximum intensity for different wheel steels, and the maximum intensity could be ranked as: EW1 > CW1 > EW2 > CW2. Furthermore, the maximum intensity in the matrix was much lower than that in the top layer. Fig. 19d and e shows that although the difference in the fractions of each type of grain was large for different wheel matrixes, the difference for different wheel top layers was small.

Based on the above analysis of Fig. 19, it can be concluded that the grain diameter, misorientation angle, preferred orientation and recrystallization in the top layer microstructure after the tests could not be affected by the difference in the wheel material matrix microstructure.

## 4. Discussion

### 4.1. Adhesion transition mechanism

In previous studies [32–34], the adhesion coefficient presented an evident decreasing tendency with the increase in sand feed rate when sanding was used in dry wheel-rail contact conditions. The main mechanism of adhesion reduction was recognized as the solid lubrication effect of sand particles. However, in this work, the variation trend of adhesion coefficient with sand deposition density for different wheel-rail material matchings (Fig. 6) could be summarized as a representative curve, as shown in Fig. 20. The curve could be divided into four segments, i.e., point A, segments AB, BC and CD. The sand deposition density values of b and c respectively corresponding to the turning points B and C might be variable for different wheel-rail material matchings. Furthermore, based on the analysis of surface roughness (Fig. 8) and surface damage (Table 3 and Figs. 10–12), the adhesion transition mechanisms in different segments could be proposed as follows.

At point A, there was no sand applied in the wheel-rail interface and

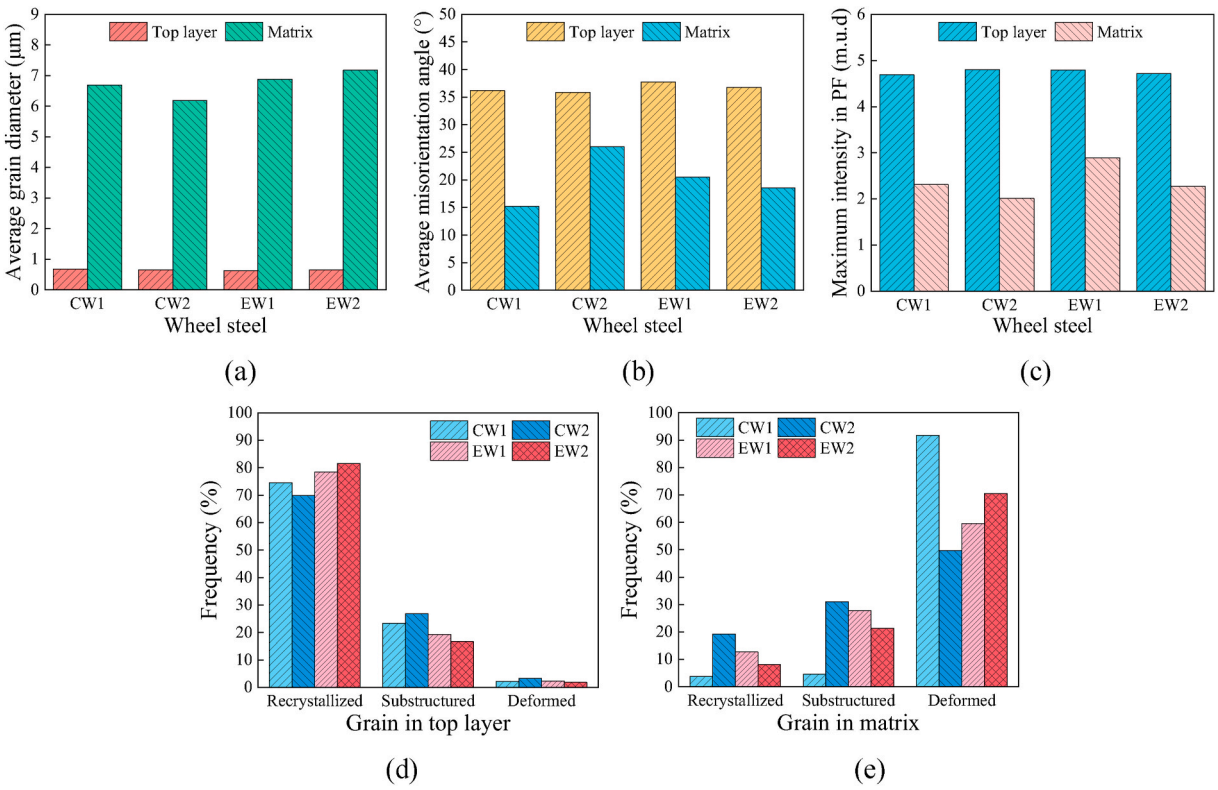


**Fig. 19.** Statistical results of EBSD analysis for different wheel steels under the sand deposition density of 3 g/m$^2$: (a) average grain diameter; (b) average misorientation angle of grain boundary; (c) maximum intensity in pole figure (PF); (d) recrystallized fraction in the top layer; (e) recrystallized fraction in the matrix.

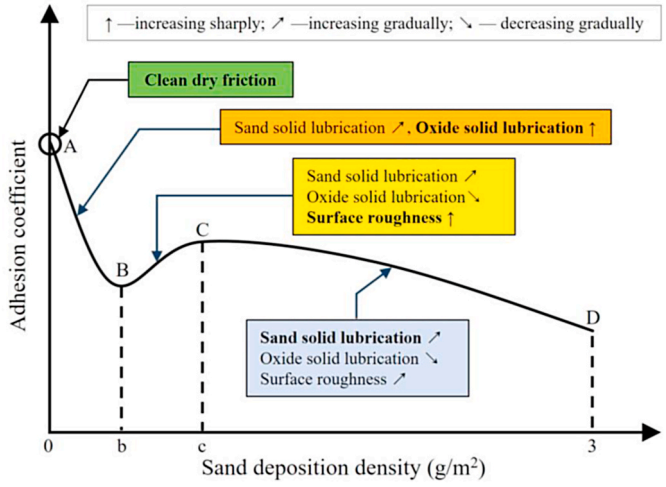


**Fig. 20.** Adhesion transition mechanisms with the increase in sand deposition density.

the adhesion coefficient was the highest. The adhesion was attributed to the clean dry friction. In segment AB, with the increase in sand deposition density, the sand solid lubrication increased gradually and the oxide ($Fe_3O_4$) solid lubrication increased sharply, which resulted in the sharp decrease in adhesion coefficient.

In segment BC, although the sand solid lubrication increased gradually, the oxide lubrication decreased gradually and the surface roughness increased sharply, which eventually resulted in the slow increase in adhesion coefficient. In addition, the sand solid lubrication and oxide solid lubrication exhibited a competitive relationship in this segment because the increase of sand particles would also accelerate the crushing and removal of oxides [24]. In segment CD, although the surface roughness increased slowly and the oxide solid lubrication decreased gradually, the sand solid lubrication increased continuously, which finally led to the slow decrease in adhesion coefficient.

### 4.2. *Wheel-rail material matching performance analysis*

Generally, anti-wear and anti-fatigue performances have always been the focus of attention of wheel and rail materials. These performances are closely related to the service environments (e.g., water, leaves, humidity, iron oxides, temperature, solid particles) [35–40] and wheel-rail material matchings [41–44]. As an extremely harsh service environment for wheel-rail materials, sand deposition on rail top had significant influences on wheel-rail service performances according to the analysis in section 3. Therefore, the selection of wheel and rail materials in the desert environment would be discussed based on the analysis of wear and fatigue performances in this experimental study.

The anti-wear performance could be evaluated by the wear rate results, i.e., the higher the wear rate, the worse the anti-wear performance. Therefore, according to the results of Fig. 7, the anti-wear performance for different wheel-rail material matchings could be ranked as: [CW1-U75V] ≈ [CW2-U75V] > [EW1-900A] > [EW2-900A]. On the other hand, the anti-fatigue performance could be evaluated by the fatigue crack depth, i.e., the larger the crack depth, the worse the anti-fatigue performance. According to the results of Fig. 15, the crack depth was relatively small (about 30 μm) for all wheel and rail steels when the sand deposition density was lower than 1 g/m$^2$. Therefore, the relatively large crack depth occurred at high sand deposition density (higher than 1 g/m$^2$) was used to evaluate the anti-fatigue performance of different wheel-rail material matchings. It can be concluded that the anti-fatigue performance for different wheel-rail material matchings could be ranked as: [CW1-U75V] > [EW2-900A] > [CW2-U75V] > [EW1-900A]. Considering the anti-wear and anti-fatigue performance comprehensively, CW1-U75V performed the best among these four types of wheel-rail material matchings in desert environments. Meanwhile, it also

indicated that in the case of wheel and rail steels with similar hardness, the wheel-rail material matching with higher carbon content had better service performance in desert sand contamination condition, which is consistent with the results in another study [10].

Furthermore, based on the results of wear rate (Fig. 7), surface damage (Figs. 10–12), plastic deformation (Fig. 14) and crack depth (Fig. 15), it can be summarized generally that the wear and damage of wheel and rail were relatively mild when the sand deposition density was lower than 0.4 g/m$^2$. It also signified that the sand deposition density on rail top should be controlled below 0.4 g/m$^2$ in desert environments to relieve the wheel-rail wear and damage based on this experimental study.

Certainly, due to the inherent limitations of twin-disc machine, the sand entering the wheel-rail interface continuously and the residue of sand fragments would result in the formation of sand recycling layers both on wheel and rail specimens' surfaces, which further caused the actual sand deposition density being higher than the quoted value. Meanwhile, the size ratio of sand particle to specimen was much larger than that of sand particle to real wheel and rail, which might lead to certain differences in sand crushing behavior. Both these factors were more likely to make the wear and damage of wheel-rail in this experimental condition more severe than in reality. On the other hand, it is known that the field desert environment is far more complex than the laboratory, e.g., wide sand particle size distribution, uneven sand deposition density, vibration of wheel-rail system, variable weather etc. Therefore, the further work should be performed on a large-scale test rig or in field trials considering more desert environmental parameters and operating parameters of train.

## 5. Conclusions

In this work, the wear and damage behaviors of wheel-rail with different material matchings under various sand deposition densities of rail top in desert environments were explored using the experimental method. Although the wear and damage of wheel-rail in this experimental condition were more likely severe than that in the field, some valuable conclusions could still be drawn, which could provide some references and ideas for the study of field wheel-rail service behavior in desert environments.

1. With the increase in sand deposition density, adhesion coefficient first decreased sharply and then increased slowly, and finally decreased slowly. The sharply decreasing trend was attributed to the combined solid lubrication effect of sand and oxide. The slowly increasing trend was attributed to the increase of wheel-rail surface roughness and the decrease of oxide solid lubrication effect. The final slowly decreasing trend was mainly caused by the increase of sand solid lubrication.
2. As the sand deposition density increased, the oxidative wear increased first, peaking at around 0.2 g/m$^2$, and then decreased, whereas the fatigue wear decreased consistently.
3. Although there was a certain difference in the material matrix microstructure for different wheel steels, the grain diameter, misorientation angle, preferred orientation and recrystallization in the top layer microstructure of different wheel steels were similar.
4. In the case of wheel and rail steels with similar hardness, the wheel-rail material matching with higher carbon content had better anti-wear and anti-fatigue performances in desert sand contamination condition.
5. The wear and damage of wheel and rail were relatively mild when the sand deposition density was lower than 0.4 g/m$^2$. It is recommended that the sand deposition density on the rail top in desert environments should be kept below 0.4 g/m$^2$ to mitigate the wheel-rail wear and damage based on this experimental study.

## CRediT authorship contribution statement

**K. Shu:** Writing – original draft, Investigation, Conceptualization. **N. Zani:** Investigation. **L. Ghidini:** Investigation. **C. Petrogalli:** Investigation. **L.L. Yu:** Investigation. **A. Mazzù:** Writing – review & editing, Supervision, Conceptualization. **H.H. Ding:** Writing – review & editing. **W.J. Wang:** Writing – review & editing.

## Declaration of competing interest

The authors declare that they have no known competing financial interests or personal relationships that could have appeared to influence the work reported in this paper.

## Acknowledgements

This work was supported by the Aid Program for Science and Technology Innovative Research Team in Higher Educational Institutions of Hunan Province (High Performance Manufacturing Processes and Service Performance Optimization) and College Students' Innovative Entrepreneurial Training Plan Program.

## Data availability

No data was used for the research described in the article.

## References

[1] L. Raffaele, L. Bruno, Windblown sand mitigation along railway megaprojects: a comparative study, Struct. Eng. Int. : journal of the International Association for Bridge and Structural Engineering 30 (2020) 355–364.
[2] K. Zhang, J. Qu, Y. Yu, Q. Han, T. Wang, Z. An, F. Hu, Progress of research on wind-blown sand prevention and control of railways in China, Adv. Earth Sci. 34 (2019) 573–583.
[3] L. Bruno, M. Horvat, L. Raffaele, Windblown sand along railway infrastructures: a review of challenges and mitigation measures, J. Wind Eng. Ind. Aerod. 177 (2018) 340–365.
[4] M.R. Hou, F.S. Liu, Z. Zhang, D. Cheng, X. Fang, Typical wheel-rail profile change and matching characteristics of high-speed railway in China, Chinese Railway, Science 41 (2020) 99–107.
[5] T. Hewitt, Designing a heavy haul desert railway: lessons learned. 11th International Heavy Haul Conference, Perth, 2015.
[6] J. Kóllmann, Railway Operations under Harsh Environmental Conditions Sand, Dust & Humidity Problems and Technical Solutions/mitigation Measures, AHK workshop be a partner of Qatar Rail, Berlin, 2013.
[7] W.R. Tyfour, Predicting the effect of grinding corrugated rail surface on the wear behavior of pearlitic rail steel, Tribol. Lett. 29 (2008) 229–234.
[8] F. He, Hundreds of workers rushed out of the car with shovels after a sandstorm caused the railway to be buried. http://news.cjn.cn/gnxw/202103/t3804521.htm, 2021. (Accessed 16 March 2021).
[9] Yiw, Railway tracks in desert. https://www.xcar.com.cn/bbs/viewthread.php?tid=92997049, 2019. (Accessed 10 September 2019).
[10] M. Faccoli, C. Petrogalli, M. Lancini, A. Ghidini, A. Mazzù, Effect of desert sand on wear and rolling contact fatigue behaviour of various railway wheel steels, Wear 396–397 (2018) 146–161.
[11] D.G. Grieve, R.S. Dwyer-Joyce, J.H. Beynon, Abrasive wear of railway track by solid contaminants, Proc. Inst. Mech. Eng. F J. Rail Rapid Transit 215 (2001) 193–205.
[12] A. Mazzù, D. Battini, N. Zani, Effect of solid contaminants on ratcheting and crack nucleation in wheel-rail contact. Proceedings of the Fifth International Conference on Railway Technology: Research, Development and Maintenance, France, 2022.
[13] A. Mazzù, A. Ghidini, N. Zani, M. Faccoli, A simplified numerical study of wheel/rail material coupling in presence of solid contaminants, Tribology - materials, Surface. Interfac. 15 (2021) 102–114.
[14] A. Mazzù, D. Battini, A model for the assessment of wheel–rail contact in the presence of solid contaminants, Tribol. Trans. 62 (2019) 230–238.
[15] K. Shu, H.H. Ding, A. Mazzù, Q. Lin, J. Guo, E. Meli, Q.Y. Liu, W.J. Wang, Effect of dynamic windblown sand environments on the wear and damage of wheel-rail under different slip ratios, Wear 500–501 (2022) 204349.
[16] M. Faccoli, C. Petrogalli, A. Ghidini, On mechanical properties of new railway wheel steels for desert environments and sand caused wheel damage mechanisms, J. Mater. Eng. Perform. 28 (2019) 2946–2953.
[17] K. Shu, H.H. Ding, Q. Lin, W.J. Wang, J. Guo, Q.Y. Liu, Effect of rail hardness on wheel-rail rolling wear and damage under the moderate sandstorm environment, J. Mech. Eng. 59 (2023) 186–197.

[18] Y. Guan, H. Zhang, B. Xiao, Z. Zhou, X. Yan, In-situ investigation of the effect of dust deposition on the performance of polycrystalline silicon photovoltaic modules, Renew. Energy 101 (2017) 1273–1284.
[19] H.K. Elminir, A.E. Ghitas, R.H. Hamid, F. El-Hussainy, M.M. Beheary, K.M. Abdel-Moneim, Effect of dust on the transparent cover of solar collectors, Energy Convers. Manag. 47 (2006) 3192–3203.
[20] N. Zani, K. Shu, L. Ghidini, C. Petrogalli, A. Mazzù, Impact of sand feed rate on the damage of railway wheel steels, IOP Conf. Ser. Mater. Sci. Eng. 1306 (2024) 012036.
[21] M.K. Nieuwoudt, J.D. Comins, I. Cukrowski, The growth of the passive film on iron in 0.05 M NaOH studied in situ by Raman micro-spectroscopy and electrochemical polarisation. Part I: near-resonance enhancement of the Raman spectra of iron oxide and oxyhydroxide compounds, J. Raman Spectrosc. 42 (2011) 1335–1339.
[22] W.T. Zhu, L.C. Guo, L.B. Shi, Z.B. Cai, Q.L. Li, Q.Y. Liu, W.J. Wang, Wear and damage transitions of two kinds of wheel materials in the rolling-sliding contact, Wear 398–399 (2018) 79–89.
[23] T. Yamashita, P. Hayes, Analysis of XPS spectra of Fe2+ and Fe3+ ions in oxide materials, Appl. Surf. Sci. 254 (2008) 2441–2449.
[24] K. Shu, W. Wang, H. Ding, Q. Lin, E. Meli, J. Guo, A. Mazzù, Q. Liu, Influence of sand transport rate on rolling wear and damage behaviors of wheel/rail in Gobi and desert windblown sand environments, Tribol. Int. 172 (2022) 107584.
[25] Y. Zhou, J.F. Peng, W.J. Wang, X.S. Jin, M.H. Zhu, Slippage effect on rolling contact wear and damage behavior of pearlitic steels, Wear 362–363 (2016) 78–86.
[26] H. Chen, C. Zhang, W. Liu, Q. Li, H. Chen, Z. Yang, Y. Weng, Microstructure evolution of a hypereutectoid pearlite steel under rolling-sliding contact loading, Materials science & engineering. A, Structural materials : properties, microstructure and processing 655 (2016) 50–59.
[27] R. Lewis, R.S. Dwyer-Joyce, Wear mechanisms and transitions in railway wheel steels, Proc. IME J. J. Eng. Tribol. 218 (2004) 467–478.
[28] Y. Zhu, The influence of iron oxides on wheel–rail contact: a literature review, Proc. Inst. Mech. Eng. F J. Rail Rapid Transit 232 (2018) 734–743.
[29] T. Shi, J. Liu, G. Yang, A. Liu, F. Liu, Effect of cyclic loading on the surface microstructure evolution in the pearlitic rail, Coatings 13 (2023) 1850.
[30] Y. Hu, L. Zhou, H.H. Ding, R. Lewis, Q.Y. Liu, J. Guo, W.J. Wang, Microstructure evolution of railway pearlitic wheel steels under rolling-sliding contact loading, Tribol. Int. 154 (2021) 106685.
[31] C.G. He, H.H. Ding, L.B. Shi, J. Guo, E. Meli, Q.Y. Liu, A. Rindi, Z.R. Zhou, W. J. Wang, On the microstructure evolution and nanocrystalline formation of pearlitic wheel material in a rolling-sliding contact, Mater. Char. 164 (2020) 110333.
[32] M. Omasta, M. Machatka, D. Smejkal, M. Hartl, I. Křupka, Influence of sanding parameters on adhesion recovery in contaminated wheel–rail contact, Wear 322–323 (2015) 218–225.
[33] O. Arias-Cuevas, Z. Li, R. Lewis, Investigating the lubricity and electrical insulation caused by sanding in dry wheel–rail contacts, Tribol. Lett. 37 (2010) 623–635.
[34] R. Lewis, R.S. Dwyer-Joyce, J. Lewis, Disc machine study of contact isolation during railway track sanding, Proceedings of the Institution of Mechanical Engineers. Part F, Journal of rail and rapid transit 217 (2003) 11–24.
[35] M. Omasta, H. Chen, Wheel-rail Interface under Extreme Conditions, Rail Infrastructure Resilience, Elsevier, 2022, pp. 137–160.
[36] M.X. Shen, Y.F. Qin, D.H. Ji, M. Yu, S.X. Li, L. Huangfu, S.P. Liu, Role of ambient temperature in the adhesion and damage characteristics of wheel/rail interface during rolling-sliding contact, Wear 506 (2022) 204458.
[37] M.X. Shen, J.Q. Li, L. Li, S.X. Li, C.Y. Ma, Adhesion and damage behaviour of wheel–rail rolling–sliding contact suffering intermittent airflow with different humidities and ambient temperatures, Tribol. Lett. 72 (2024) 18.
[38] K.J. Rong, Y.L. Xiao, M.X. Shen, H.P. Zhao, W.J. Wang, G.Y. Xiong, Influence of ambient humidity on the adhesion and damage behavior of wheel–rail interface under hot weather condition, Wear 486–487 (2021) 204091.
[39] Y. Zhu, W. Wang, R. Lewis, W. Yan, S.R. Lewis, H. Ding, A review on wear between railway wheels and rails under environmental conditions, J. Tribol. 141 (2019) 1–37.
[40] U. Olofsson, Y. Lyu, Open system tribology in the wheel–rail contact—a literature review, Appl. Mech. Rev. 69 (2017) 060803.
[41] H.G. Yenealem, D.T. Redda, A. Mohammedseid, The effect of hardness matching of rail/wheel materials on wear rate of railway wheel, Engineering Solid Mechanics 11 (2023) 271–280.
[42] X.J. Shi, X.X. Zhang, G.J. Diao, Q.Z. Yan, Wear behavior of high-speed wheel and rail steels under various hardness matching, J. Mater. Eng. Perform. 32 (2023) 366–380.
[43] Y. Hu, M. Watson, M. Maiorino, L. Zhou, W. Wang, H. Ding, R. Lewis, E. Meli, A. Rindi, Q. Liu, Experimental study on wear properties of wheel and rail materials with different hardness values, Wear 477 (2021) 203831.
[44] X. Shi, Q. Yan, X. Zhang, G. Diao, C. Zhang, Z. Hong, Z. Wen, X. Jin, Hardness matching of rail/wheel steels for high-speed-train based on wear rate and rolling contact fatigue performance, Mater. Res. Express 6 (2019) 066501.